NeuroImage 47 (2009) 1244–1251

Contents lists available at ScienceDirect

NeuroImage

journal homepage: www.elsevier.com/locate/ynimg

In vivo diffusion tensor imaging of the human optic chiasm at sub-millimeter resolution

Joelle E. Sarlls *, Carlo Pierpaoli

National Institute of Child Health and Human Development, National Institutes of Health, Bethesda, Maryland, USA

ARTICLE INFO

Article history:
Received 31 December 2008
Revised 28 May 2009
Accepted 29 May 2009
Available online 9 June 2009

ABSTRACT

In this work we report findings from an *in vivo* diffusion tensor imaging (DTI) study of the human optic chiasm at sub-millimeter voxel resolution. Data were collected at 3 T using a diffusion-weighted radial-FSE sequence, which provides images free from typical magnetic susceptibility artifacts. The general DTI features observed in the optic chiasm region were consistent across subjects. They included a central area with high anisotropy and highest diffusivity in a predominately right/left direction corresponding to the decussation of nasal hemiretinae fibers, surrounded by a band of low anisotropy reflecting heterogeneous orientation of fibers within the voxel, and a lateral area with high anisotropy and highest diffusivity in a predominately anterior/posterior direction corresponding to temporal hemiretinae fibers that do not cross. Animal studies indicate that there is a significant dorsal–ventral reorganization of the retinotopic distribution of fibers along the optic pathways. We found that diffusion ellipsoids in the central portion of the optic chiasm show considerable planar anisotropy in the coronal plane indicating fiber crossings in the superior/inferior direction, rather than strictly right/left. This architectural feature of the chiasm suggests that dorso–ventral reorganization of fibers in the optic pathways also occurs in humans. We have shown that by collecting sub-millimeter resolution data, DTI can be used to investigate fine details of small and complex white matter structures, *in vivo*, with a clinical scanner. High spatial resolution, however, is necessary in the slice direction as well as in-plane to reduce the CSF contribution to the signal and to increase fiber coherence within voxels.

Published by Elsevier Inc.

Introduction

The optic chiasm is a challenging structure to image *in vivo* with diffusion-weighted MRI (DWI) methods due to its small size (~12×8×4 mm) and to its proximity to air/tissue interfaces, blood vessels, and cerebrospinal fluid (CSF). It is worth overcoming these challenges for several reasons. First, the chiasm has an intricate white matter architecture, the general features of which are anatomically well characterized, which makes it interesting to study with diffusion tensor imaging (DTI). The architecture of the chiasm may be an important factor in studying the development of the visual system as it is an area indicated in several developmental mechanisms and varies between mammalian species (Jeffery, 2001). Second, there are several clinically driven motivations for this study. Extrinsic pathology in the sellar region, including pituitary adenomas, meningiomas, craniopharyngiomas, and aneurysms, commonly produces visual field deficits due to compression of the optic chiasm (Muller-Forell, 2004). DTI may be useful in documenting reversible versus irreversible damage to the visual pathways. Intrinsic pathology, including radiation induced optic neuropathy, multiple sclerosis, and optic pathway gliomas, can also be studied with DTI. For example, early stage optic pathway gliomas can be difficult to diagnose as they may not enhance with contrast agents and may not induce changes in T1- or T2-weighted images. However, even a very small glioma will compromise the coherence of fiber pathways and should induce changes in DTI parameters. These changes may provide a means of localizing and monitoring the lesion.

Studying the chiasm with diffusion tensor methods requires a sequence that provides high spatial resolution without susceptibility artifacts. Different methods have been developed with this aim and used for *in vivo* optic nerve and/or chiasm DTI studies (Chabert et al., 2005; Vinogradov et al., 2005; Trip et al., 2006; Wheeler-Kingshott et al., 2006). Each method has its benefits and drawbacks; however, apparently none have been used to acquire DTI with a voxel volume less than 1.8 mm^3. We have recently developed a radial fast spin-echo (FSE) sequence for high-resolution DTI of *in vivo* brain at 3 T that allows sub-millimeter isotropic voxels to be acquired in areas of strong magnetic field inhomogeneity (Sarlls and Pierpaoli, 2008).

In this work we have performed both inter- and intra-subject DTI of the optic chiasm utilizing the diffusion-weighted radial-FSE sequence. Exploratory studies were performed to understand the effect of in-plane resolution and slice thickness on the calculated DTI parameters. In addition, data sets were analyzed to extract general DTI features of the optic chiasm.

* Corresponding author. National Institutes of Health, Building 13, Room 3W16, 13 South Drive, Bethesda, MD 20892, USA. Fax: +1 301 435 5035.
E-mail address: sarllsjo@mail.nih.gov (J.E. Sarlls).

1053-8119/$ – see front matter. Published by Elsevier Inc.
doi:10.1016/j.neuroimage.2009.05.098

Materials and methods

The diffusion-weighted radial-FSE sequence utilized in this study contains a spin-echo diffusion preparation period followed by a train of 180° RF refocusing pulses. An individual radial line (view) is collected at each spin-echo point in the echo train with all gradients refocused before each successive 180° RF pulse. To combat the violation of the CPMG condition in diffusion-weighed MRI, a mixed-CPMG phase cycling scheme was implemented (Pipe et al., 2002). In addition, a refocusing slice thickness that is 300% of the excitation slice was implemented to improve the B1 homogeneity at higher fields, as described in (Pell et al., 2006). All radial-FSE data were collected with bit-reversed view ordering to minimize streaking artifacts (Theilmann et al., 2004). To combat shot-to-shot phase variations, images acquired with radial-FSE were reconstructed by magnitude filtered back projection (Trouard et al., 1999).

Healthy male volunteers (aged 31 to 46) were scanned under an approved protocol. All data were collected on a GE Signa 3 T scanner with maximum gradient strength of 40 mT/m and slew rate of 150 T/m/s. Either an 8-channel or 16-channel phased array coil was used for data collection depending on which coil was available at the time of scanning. The measured signal-to-noise ratio (SNR) in the region of the optic chiasm was similar for both coils. The imaging protocol contained a 3-plane localizer followed by a 1 mm isotropic T1-FLAIR volume acquired in the sagittal plane. These images were then used for planning optic chiasm imaging. Contiguous T1-FLAIR images were aligned with the angle of the optic chiasm, typically with a pitch between −10° and −20° from the axial plane, and collected at the voxel dimensions desired for DTI data collection. The slice that most fully encompassed the optic nerves, optic chiasm, and optic tracts was then chosen for the DTI acquisition.

When an oblique slice is collected, the diffusion gradients are also rotated through the same angle to remain in the reference frame of the imaging plane. The oblique imaging plane is described by the read (R)–phase (P)–slice (S) coordinate system, corresponding to (*X*, *Y*, *Z*) for an axial slice. The DTI data sets contain one non-diffusion-weighted image and DWIs in the following six non-collinear directions: (R, P), (P, S), (R, S), (−R, P), (−P, S), and (−R, S). Because the maximum target gradient strength available is automatically adjusted dependant on the angle of the oblique plane, the gradient strength actually played out on each gradient axis was written to a file for every scan. This information was then taken into account in the calculation of the *b*-matrix, in the RPS reference frame, using in-house IDL code based on the theory developed by Mattiello et al. (1997). All radial-FSE data had a diffusion preparation period with $\delta = 17.3$ ms and $\Delta = 31$ ms, which yields a *b*-value ~1100 s/mm^2.

When imaging over a limited volume, through-plane motion can be devastating as the object of interest can be removed from the acquired slice and not located in an adjacent slice, rendering the data set useless for DTI analysis. Thus, it is critical to keep subject motion to a minimum throughout the total scan time. To aid in immobilizing the head, disposal bite bars were constructed and fastened to the receiving coil with tape.

Effects of sequence type and resolution in DTI of the optic chiasm

For comparison, data were collected on a healthy volunteer with diffusion-weighted single-shot echo planar imaging (SSEPI) and diffusion-weighted radial-FSE. The SSEPI data were acquired in 16.8 min with the following scan parameters: TE/TR = 85/6000 ms, FOV = 25 cm, 128×128, 2 mm slice thickness, NEX = 4, SENSE factor = 2, and reconstructed at 256×256. The slice was then acquired at the same 2 mm isotropic resolution with radial-FSE, in 18.66 min, using the following scan parameters: TE/TR = 68/2500 ms, FOV = 25 cm, steps = 128, views = 256, ETL = 4, RBW = ±16 kHz, 2 mm slice thickness, and reconstructed at 256×256. Keeping the location of the center of the slice constant, data were acquired at 0.9 mm isotropic resolution with radial-FSE using the following scan parameters: TE/TR = 68/2500 ms, FOV = 23 cm, steps = 256, views = 512, ETL = 4, RBW = ±16 kHz, and 0.9 mm slice thickness for a total scan time of 37.33 min. Recall that for data collected on a polar grid the image resolution is determined by the imaging FOV and number of sample points per view only.

Effects of slice thickness in high-resolution DTI of the optic chiasm

To test the effects of slice thickness data were acquired of a healthy volunteer with high in-plane resolution, 0.8×0.8 mm, at 3 mm and 0.8 mm slice thickness. Data were acquired using the following scan parameters: TE/TR = 68/2500 ms, FOV = 22 cm, steps = 256, ETL = 4, RBW = ±16 kHz, and views = 384 and 512 for the 3 mm and 0.8 mm slice thickness data sets, respectively.

Repeated sub-millimeter radial-FSE DTI in the same subject

One healthy volunteer underwent the high-resolution DTI protocol during three separate scan sessions. In the first two scan sessions, data were acquired at 0.9 mm isotropic resolution with radial-FSE using the following scan parameters: TE/TR = 68/2000 ms, FOV = 23 cm, steps = 256, views = 512, ETL = 4, RBW = ±16 kHz, and 0.9 mm slice thickness. In the third scan session, we added cardiac gating and increased the number of views to 640 to see if these changes would further improve data quality. Peripheral gating was used over 3 R×R periods with a minimum trigger delay. The subject's heart rate was ~65 BPM, yielding a TR ~ 2770.

Sub-millimeter radial-FSE DTI with a typical clinical setup

An additional seven healthy volunteers underwent the high-resolution DTI protocol without the bite bar restraint to test the clinical feasibility of such a protocol. Data were acquired at 0.9 mm isotropic resolution using the following scan parameters: TE = 68 ms, FOV = 23 cm, steps = 256, views = 640, ETL = 4, RBW = ±16 kHz, 0.9 mm slice thickness and peripheral gating over 3 R×R periods with a minimum trigger delay.

Diffusion tensor image processing

From the diffusion-weighted data, the diffusion tensor (Basser et al., 1994) was computed by non-linear least squares fitting using IDL code developed in-house. This provides the eigenvectors and eigenvalues, which represent the direction and magnitude of the principle diffusivities. The eigenvalues were sorted in order of decreasing magnitude to provide the first, second, and third eigenvalues (λ_1, λ_2, λ_3) and their corresponding eigenvectors (ε_1, ε_2, ε_3). The orientationally-averaged mean diffusivity, $\langle D \rangle$ (Basser et al., 1994), which is equal to 1/3 of the Trace of the diffusion tensor, the fractional anisotropy (FA) (Basser and Pierpaoli, 1996), and the lattice anisotropy index (LI) (Pierpaoli and Basser, 1996) were calculated on a voxel-by-voxel basis. Conventional directionally encoded color (DEC) maps, with color corresponding to ε_1 and scaled by LI, were also derived from the DTI data and are referred to as LI-ε_1 DEC maps in this work (Pajevic and Pierpaoli, 1999).

In order to study microstructural characteristics of various fiber populations, within or across subjects, it is useful to analyze regions of interest (ROIs). An ROI was chosen on the LI-ε_1 DEC map that encompassed the central portion of the optic chiasm in each data set. Average diffusion parameters, along with the non-diffusion-weighted signal intensity, were measured. The SNR in the central chiasm region was calculated using the method proposed by Koay and Basser (2006) taking into account the signal intensity of the non-diffusion-weighted

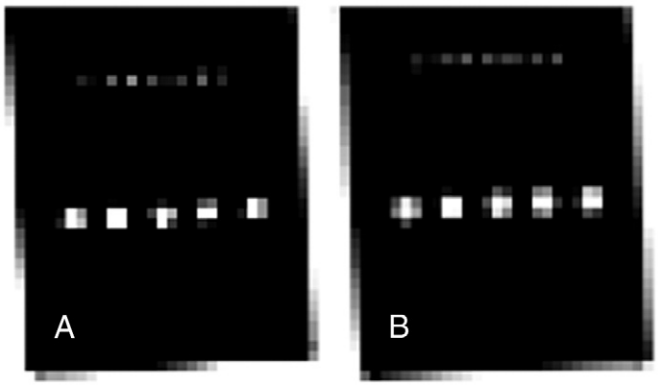

Fig. 1. Images of a resolution phantom acquired with a standard FSE (A) and the radial-FSE (B) sequence at 0.9 × 0.9 mm in-plane resolution. The images have been cropped to the area of pertinent resolution. The large squares are 2 × 2 mm with 2 mm spacing, while the smaller squares are 1 × 1 mm with 1 mm spacing.

data in the region, the standard deviation of the underlying Gaussian noise in a large region, and the number of receiver coils. To characterize architectural features of fibers within the ROI we computed the average eigenvectors using the method proposed by Basser et al. which is based on a dyadic tensor representation (Basser and Pajevic, 2000). In addition, to obtain measures of the dispersion of the average eigenvectors within an ROI, the circumference and area of the elliptical cone of uncertainty was calculated (Koay et al., 2007, 2008).

Resolution phantom imaging

A multipurpose MRI phantom (Nuclear Associates Model 76-903) filled with distilled water was scanned to verify the ability of the radial-FSE sequence to achieve sub-millimeter resolution. For comparison, the product FSE sequence was used to acquire a single slice with 0.9 mm isotropic resolution with the following scan parameters: TE/TR = 83/3000 ms, FOV = 23 cm, 256 × 256, ETL = 16, and RBW = ± 32 kHz. The same slice was then acquired at 0.9 mm isotropic resolution using the high-resolution radial-FSE protocol, without diffusion weighting, with the following scan parameters: TE/TR = 68/3000 ms, FOV = 23 cm, steps = 256, views = 512, ETL = 4, and RBW = ± 16 kHz.

Results

Resolution phantom imaging

In Figs. 1A and B images of the resolution phantom acquired at 0.9 mm isotropic resolution with FSE (A) and radial-FSE (B), are shown cropped to the area of pertinent resolution. The large squares are 2 × 2 mm with 2 mm spacing, while the smaller squares are 1 × 1 mm with 1 mm spacing. It can be seen that the image reconstructed from the radial-FSE data does indeed resolve the 1 × 1 mm resolution. This is also true for the product FSE data.

Effects of sequence type and resolution in DTI of the optic chiasm

Fig. 2 shows the effects of the imaging sequence and image resolution for DTI of the optic chiasm. These images have been cropped to the optic nerves, chiasm, and tracts area of interest. In the acquired T1-FLAIR image shown for anatomical reference, Fig. 2A, and the cropped version, Fig. 2E, the entering optic nerve, optic chiasm, and exiting optic tracts are clearly visible. It is reasonable to expect the $\langle D \rangle$ of the optic nerves, chiasm, and tracts to be similar to that of parenchymal white matter, around 0.7×10^{-3} mm^2/s (Pierpaoli et al., 1996). If white matter and CSF both contribute to the signal in a voxel, then the $\langle D \rangle$ will increase dependant on the amount of CSF partial volume. Therefore, in structures surrounded by CSF it is logical to assume that lower $\langle D \rangle$ corresponds to less partial volume. To analyze the effects of partial volume in the different DTI acquisitions, an ROI was measured in the right optic tract and central optic chiasm of the calculated diffusion parameter maps; the results are summarized in Table 1. In the SSEPI image, the optic nerves are not visible due to susceptibility artifacts from nearby air/tissue interfaces (Fig. 2B). The optic tracts are visible; however, $\langle D \rangle$ from the ROI of the right optic tract is corrupted by CSF contamination (see Table 1). This effect is even more severe in the optic chiasm region. The 8 mm^3 radial-FSE image, shown in Fig. 2C, does not have susceptibility artifacts. The optic nerve, chiasm, and tracts can be seen, however, the $\langle D \rangle$ from an ROI in the right optic tract and central optic chiasm are biased due to partial volume effects. Conversely, in Fig. 2D, when the radial-FSE method is used to acquire data with a voxel volume of 0.729 mm^3, which is smaller by a factor of 10, partial volume effects are dramatically reduced allowing for the measurement of more accurate mean diffusion values, which are approaching that of parenchymal

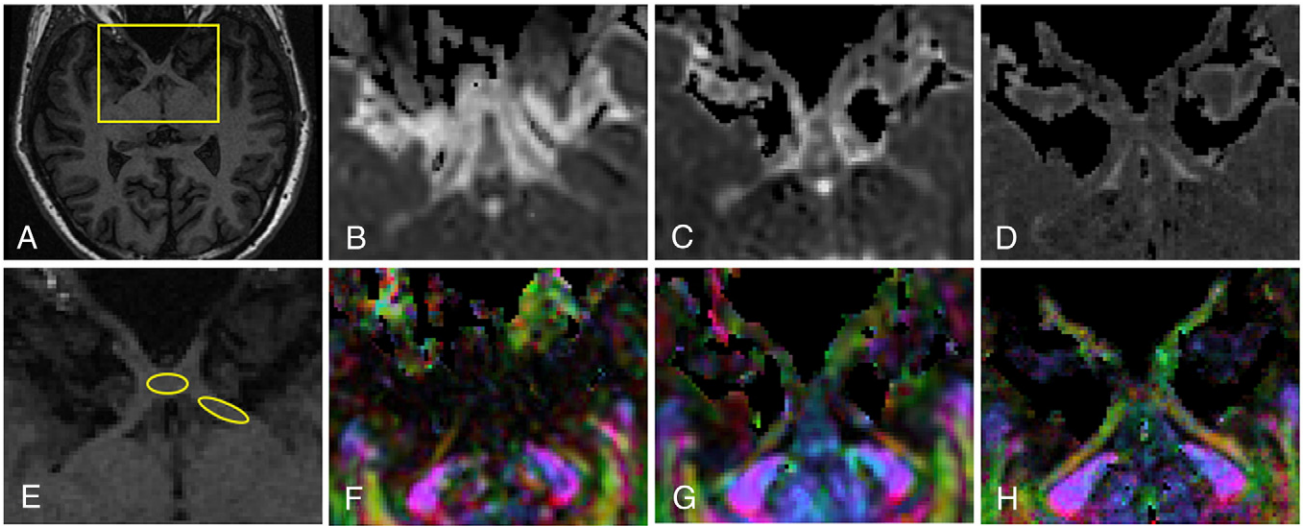

Fig. 2. Images of the optic nerves, chiasm, and tracts region in a healthy volunteer. The acquired T1-FLAIR image is shown in A for general anatomical reference. The cropped T1-FLAIR image is shown in E overlaid with representative ROIs. Corresponding mean diffusivity (B–D) and LI-ε_1 DEC (F–H) maps are displayed. Images with 8 mm^3 voxels were collected with SSEPI (B and F) and radial-FSE (C and G). Images with 0.729 mm^3 voxels acquired with radial-FSE are shown in D and H.

Table 1
ROI analysis results of diffusion parameter measures from the central optic chiasm and right optic tract of DTI data acquired with different sequence types and resolution.

	Right optic tract		Central optic chiasm	
	$\langle D \rangle$ (mm^2/s)	FA	$\langle D \rangle$ (mm^2/s)	FA
SSEPI (8 mm^3)	2.5×10^{-3}	0.28	3.1×10^{-3}	0.18
Radial-FSE (8 mm^3)	1.7×10^{-3}	0.40	1.5×10^{-3}	0.36
Radial-FSE (0.729 mm^3)	0.88×10^{-3}	0.75	1.08×10^{-3}	0.48

white matter (see Table 1). Such a reduction in voxel volume also dramatically reduces the SNR. In the region of the central optic chiasm the SNR is 55.7, 65.1, and 30.0 for the SSEPI, 8 mm^3 radial-FSE and 0.729 mm^3 radial-FSE, respectively.

The effects of a reduced voxel volume are twofold for FA measures. Because diffusion of CSF surrounding the chiasm is relatively isotropic, when there is CSF partial volume FA will be artificially decreased. In addition, reduction of partial volume from surrounding tissue leads to more coherent fiber orientation within each voxel (Pierpaoli et al., 1996). Such partial volume effects are observed in the acquired data shown in Fig. 2. Low FA was measured in the right optic tract and central chiasm of the SSEPI image (see Table 1). The 8 mm^3 radial-FSE image had higher measured FA values. An even greater improvement is observed with the radial-FSE data acquired at a voxel volume of 0.729 mm^3. At sub-millimeter resolution, the measured FA values indicate a considerable reduction in partial volume effects and are consistent with white matter.

Figs. 2F–H show the LI-ε_1 DEC maps corresponding to the mean diffusivity images in Figs. 2B–D. Clearly, at higher image resolution with the radial-FSE sequence, not only can one visualize the optic pathway structures, but tissue features within the chiasm as well. The optic nerve fibers originating from the temporal hemiretinae, which do not cross in the chiasm, remain on the ipsilateral side and appear green, running in the anterior/posterior direction. The fibers originating from the nasal hemiretinae that cross to the contralateral side can be seen in red, running in the right/left direction. In addition, the optic tracts change from green to orange as they diverge dorsolaterally.

The line field map shown in Fig. 3 displays projections of the first eigenvector of the diffusion tensor data corresponding to Fig. 2H, scaled by LI. The ipsilateral fiber pathway on the right can be followed from the optic nerve, through the optic chiasm, into the optic tract, and curving medially around the cerebral peduncle to where it enters the lateral geniculate body (arrow). The decussating fiber pathway that begins in the right optic nerve can also be followed as it traverses the optic chiasm in a mainly right/left (R/L) direction to enter the contralateral optic tract. It is important to note that the data is displayed at its collected resolution and has not been processed with a fiber tracking algorithm. This map simply shows the first eigenvector for each voxel projected onto the slice plane.

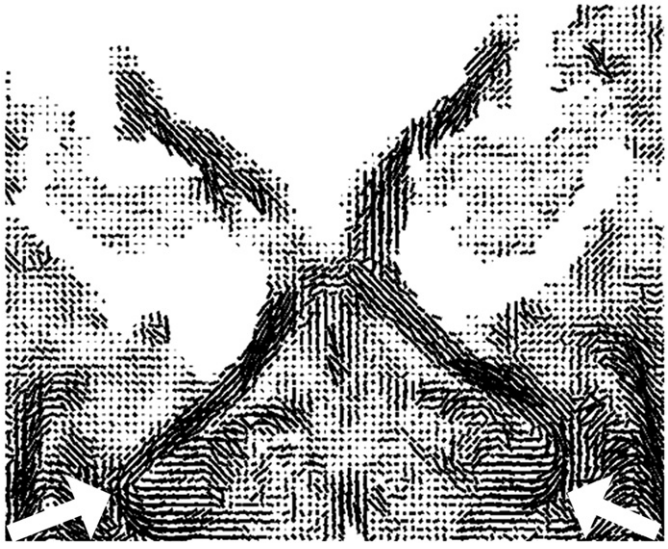

Fig. 3. Line field map, corresponding to the LI-ε_1 DEC map in Fig. 2H, displaying a segment whose length is proportional to anisotropy with orientation of the first eigenvector projected on to the slice plane. Map displays one segment per voxel at the original resolution. Arrows point to the fibers entering the lateral geniculate bodies.

Effects of slice thickness in high-resolution DTI of the optic chiasm

As mentioned in the Introduction, the optic chiasm is 4 mm thick in the dorsal/ventral direction. As a 3 mm thick slice is used for typical clinical imaging protocols of the optic chiasm, with high in-plane resolution, it is worthwhile determining if a similar approach would be suitable for DTI. Fig. 4 shows the LI-ε_1 DEC maps resulting from DTI data collected from a subject with the same in-plane resolution but with a 3 mm, A, and 0.8 mm, B, slice thickness yielding voxel volumes of 1.92 mm^3 and 0.512 mm^3, respectively. As expected, the larger slice thickness results in increased SNR, 58.2 vs. 31.3, but also a loss of structural detail within the optic chiasm. This loss of detail is probably caused by varied, rather than coherent, crossing patterns in the fiber bundles throughout the thickness of the optic chiasm. In Fig. 4A three voxels exhibit the red color indicative of the R/L orientation of the centrally crossing fibers. Fig. 4B contains six times as many red voxels in the region of the medial decussation. In addition, this region, as shown in Fig. 4A, appears to be affected by CSF partial volume and has $\langle D \rangle = 1.5 \times 10^{-3}$ mm^2/s and FA = 0.35 in the central optic chiasm. When an 0.8 mm slice thickness is used, the central optic chiasm has $\langle D \rangle = 1.2 \times 10^{-3}$ mm^2/s and FA = 0.50.

Repeated sub-millimeter radial-FSE DTI in the same subject

Fig. 5 shows results of intra-subject scanning from data collected on three separate occasions from a healthy volunteer. The LI-ε_1 DEC maps from the three scan sessions are shown in Fig. 5 ordered from the most dorsal, 5A, to the most ventral, 5C, levels. The general DTI features observed in every sub-millimeter data set in this study are present at all levels of the optic chiasm shown in Fig. 5: 1) temporal fibers that remain on the ipsilateral side appear green, 2) nasal fibers that cross to the contralateral side appear red in the central chiasm, 3) perimeter of low anisotropy around the red medial decussation. The perimeter of low anisotropy around the red medial decussation is a constant finding in our sub-millimeter optic chiasm DTI data. This finding is consistent with complex patterns of fiber crossing,

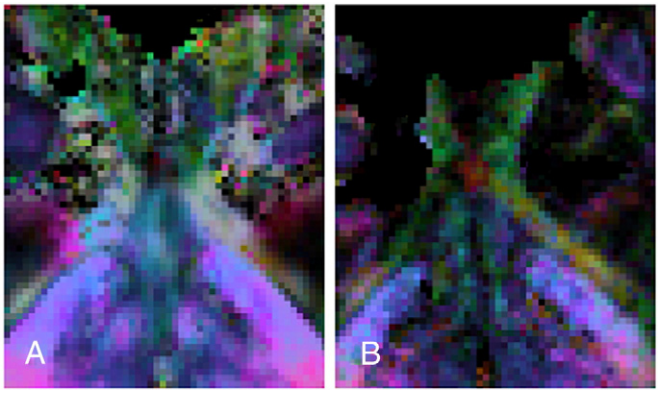

Fig. 4. LI-ε_1 DEC maps collected at the same in-plane resolution, 0.8 × 0.8 mm, with slice thickness of 3 mm (A) and 0.8 mm (B), respectively.

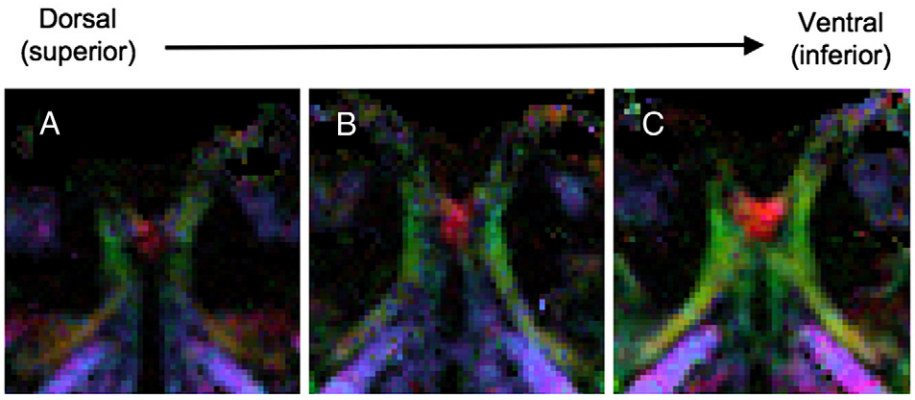

Fig. 5. LI-ε_1 DEC maps of a healthy volunteer from three separate scan sessions, all acquired at 0.9 mm isotropic resolution.

diverging, and converging in the lateral aspects of the medial chiasm presented in anatomy texts. Recall, if a voxel contains fibers with multiple orientations then that voxel will exhibit lower anisotropy. An ROI measured in the central optic chiasm of each data set yields $\langle D\rangle = 1.02\times10^{-3}$, 1.04×10^{-3}, and 0.95×10^{-3} mm^2/s, FA = 0.49, 0.59, and 0.72, and SNR = 27.9, 24.7, and 27.3 for the data sets shown in Figs. 5A–C, respectively.

In addition to scalar measures of diffusion, like $\langle D\rangle$ and FA, one can also extract information about the shape of the diffusion ellipsoid, i.e., prolate (cigar shaped), oblate (pancake shaped), and spherical (Pierpaoli et al., 1996). Westin et al. proposed quantitative measures to evaluate the degree to which the calculated diffusion ellipsoid was prolate, oblate, or spherical (Westin et al., 2002). The shape measures were defined as linear, $C_l = (\lambda_1 - \lambda_2)/\lambda_1$; planar, $C_p = (\lambda_2 - \lambda_3)/\lambda_1$; and spherical, $C_s = \lambda_3/\lambda_1$. In Fig. 6 color representations of the linear and planar diffusion components are shown for the data sets presented in Fig. 5, similar to that proposed by Zhang et al. (2006). In the C_l-ε_1 DEC maps shown in Figs. 6A–C, the direction of the primary eigenvector, ε_1, is assigned the corresponding color and has intensity proportional to C_l. In the C_p-ε_3 DEC maps shown in Fig. 6D–F, the direction perpendicular to the plane, along the direction of the third eigenvector, ε_3, is assigned the corresponding color and has an intensity proportional to C_p. At all levels of the central chiasm there is not only a strong linear anisotropy component, but a strong planar anisotropy component as well. This central planar region encompasses part of the perimeter of low anisotropy seen in the LI-ε_1 DEC maps of Fig. 5. In Fig. 6A, B, and C the linear component at the medial decussation is red and the lateral chiasm is green. In the planar maps, Figs. 6D and E, the more superior slices contain a central green region, indicating fibers crossing in the coronal plane. A schematic drawing is provided in Fig. 7 to convey the novel information of the fiber trajectories that the linear and planar anisotropy components provide. Looking at a midline region of the central chiasm from an axial view, fiber trajectories would be almost entirely R/L. Looking from a coronal view, fiber trajectories would have an R/L and an

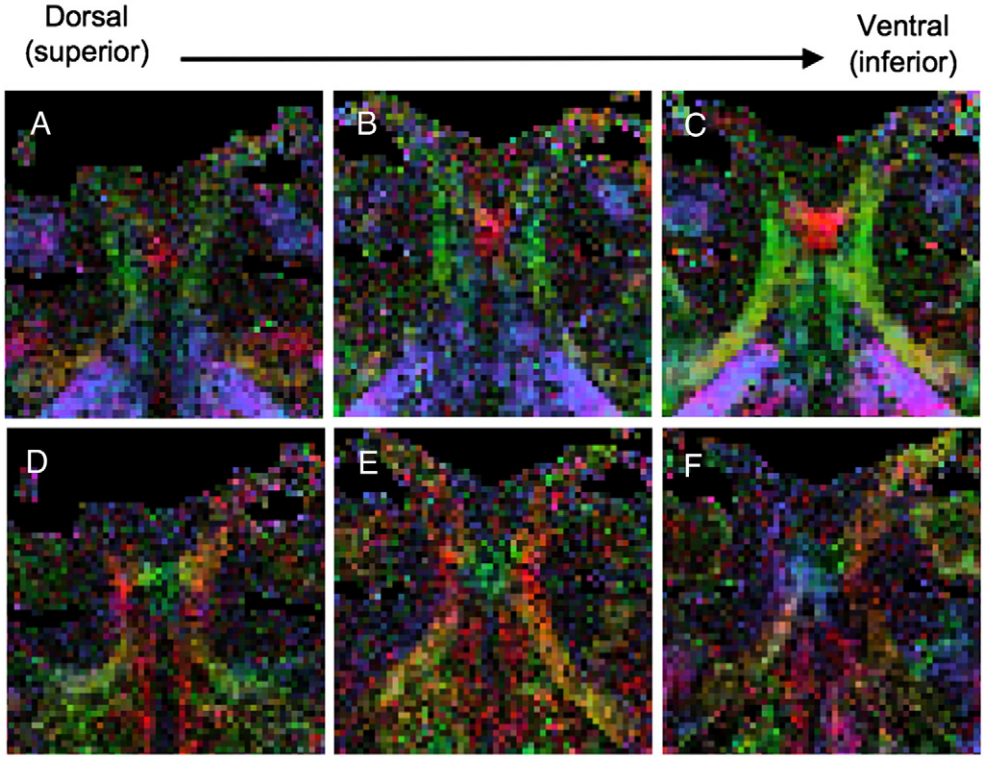

Fig. 6. Maps of linear and planar measures corresponding to the DTI data shown in Fig. 5. The C_l-ε_1 DEC maps (A–C) are color-coded with the direction of ε_1. The C_p-ε_3 DEC maps (D–F) are color-coded with the direction of ε_3, which is perpendicular to the plane.

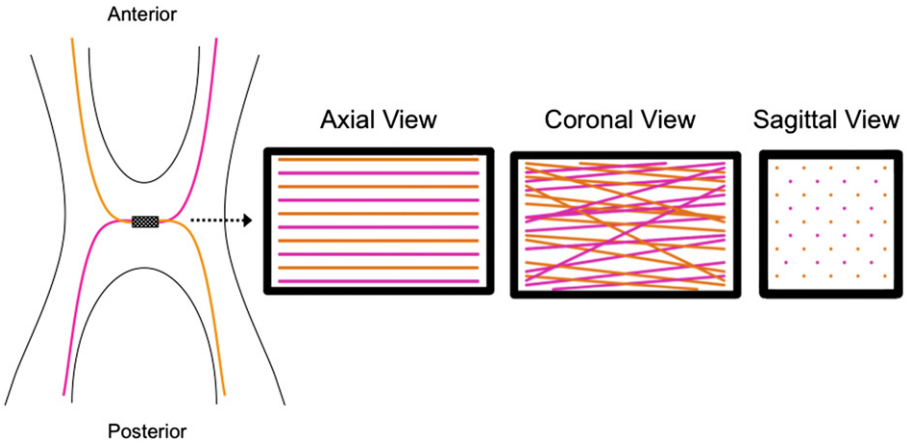

Fig. 7. Schematic of the proposed crossing trajectory pattern in the central chiasm. The pattern is shown from the three orthogonal views: axial, coronal, and sagittal. The coronal view illustrates that there is a superior/inferior component to the trajectory consequent of the topological rearrangement of fibers from the optic nerve to optic tract.

S/I component. Looking from a sagittal view, fiber trajectories would be directly in/out of the plane. The superior/inferior component to the trajectory, illustrated by the coronal view, is consistent with the topological rearrangement of fibers from the optic nerve to optic tract described in anatomy texts.

Furthermore, the most inferior slice (Fig. 6F) contains a central region that is more bluish in color, indicating fibers crossing in a plane with a pitch in the A/P direction from coronal. To further illustrate the information attained from the C_p-ε_3 DEC maps, ROIs that encompass the red voxels in the LI-ε_1 DEC maps of the central chiasm were analyzed. The planar anisotropy component was similar in Figs. 6D–F ($C_p = 0.33$, 0.31, and 0.27, respectively). However, the orientation of the third eigenvector, which is perpendicular to the plane of crossing fibers, is different. The mean third eigenvector and corresponding cone of uncertainty calculated from the ROIs are presented in Fig. 8. In all three slices, ε_3 lies in a sagittal plane. In the most superior slice, Fig. 8A, ε_3 has virtually no component in the S/I direction, being essentially collinear to the A/P axis (intersection of the imaging plane with a sagittal plane). It can be seen that, as the slices become more inferior, ε_3 exhibits an increasing component in the S/I direction. For the most inferior slice, Fig. 8C, the angle between ε_3 and the imaging plane is 41°. In addition, it can be seen from the shape of the cones that within the ROIs there is a greater dispersion of ε_3 orientation in the S/I direction compared to the R/L direction, where there is more orientational coherence.

Sub-millimeter radial-FSE DTI with a typical clinical setup

To test if the high-resolution radial-FSE DTI protocol results were reproducible under a typical clinical setup, seven additional subjects were scanned without restraint from the bite bar. Of the seven data sets collected with the high-resolution radial-FSE DTI protocol without restraint, only three maintained a constant position of the prescribed slice covering the optic chiasm throughout the acquisition. Calculated diffusion parameter maps of these three data sets confirmed the general features of the optic chiasm previously described. In total there were seven usable data sets collected with 0.729 mm^3 voxels. An ROI was defined in the central portion of the optic chiasm for all seven datasets and the mean value and standard deviation of multiple diffusion parameters for the population were computed, as summarized in Table 2.

Discussion

There have been very few studies intended to discover the exact fiber ordering through the optic chiasm in humans. The pathway of divergence of the nasal hemiretinae fibers away from the lateral hemiretinae fibers and the fibers' trajectories through the central chiasm are still unknown. However, our findings are consistent with recent publications on human optic chiasm (Neveu et al., 2006; Roebroeck et al., 2008). In the work by Roebroeck et al. of ultra high-

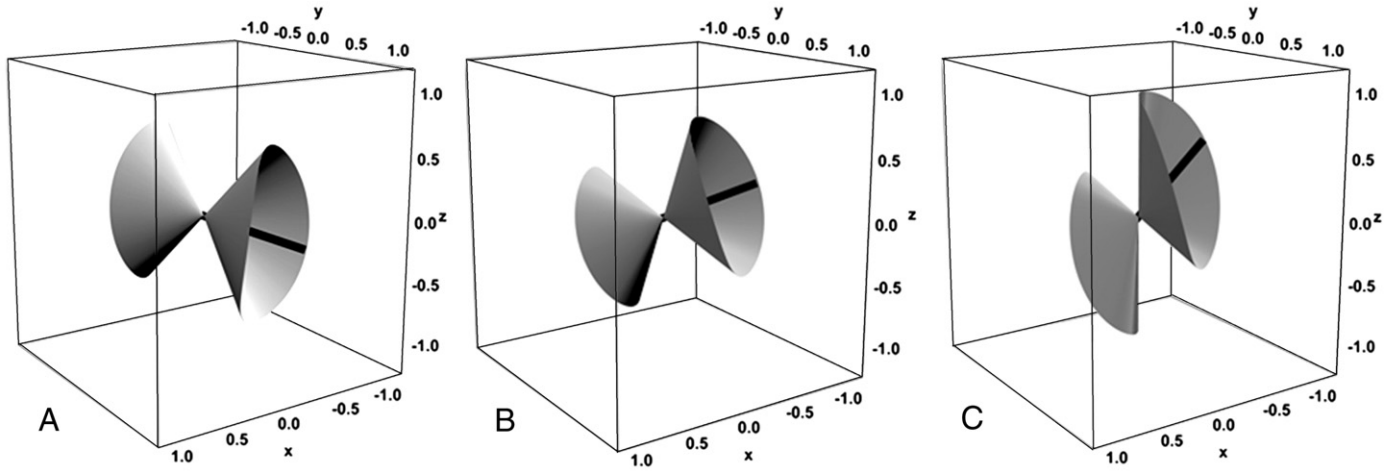

Fig. 8. Depiction of the average ε_3 corresponding to an ROI encompassing the red voxels in the central chiasm from the DTI data shown in Fig. 5 A–C. The average ε_3 is represented by the black line in the center of the corresponding cone of uncertainty, a measure of dispersion of the averaged eigenvectors.

Table 2
The mean and standard deviation of average diffusion parameter measures from the central optic chiasm region of the seven data sets acquired with 0.9 mm isotropic resolution.

	$\langle D \rangle$ (mm^2/s)	FA	LI	C_l	C_p
Mean	1.01×10^{-3}	0.57	0.37	0.42	0.33
Std dev	0.07×10^{-3}	0.10	0.12	0.13	0.07

resolution DTI of *ex vivo* human optic chiasm, two zones of complex fiber architecture were observed in the lateral central chiasm. They may likely represent the regions where nasal hemiretinae fibers diverge from the ipsilateral optic nerve and where crossed fibers merge into the contralateral optic tract. The zones were described as diagonal bands running bilaterally from the anterior and ventral aspect to the posterior and dorsal aspect of the chiasm. The consistent perimeter of low anisotropy around the medial decussation observed in our *in vivo* optic chiasm data agrees well with their finding. Indeed, the perimeter of low anisotropy seen in Fig. 5C has a clear diagonal contour.

In the histological study by Neveu et al., transverse sections show that the lateral optic chiasm contains parallel groups of fibers running in the A/P direction, while the central chiasm has interdigitated groups of fibers coursing mainly in the R/L direction. These data confirm the anatomically well-characterized structure of the optic chiasm. Accordingly, in the most central and lateral regions one would predict the direction of the primary eigenvector to be in the R/L and A/P directions, respectively, which is seen in all the sub-millimeter DTI data presented. Interestingly, a coronal section of histology from the midline region of the chiasm shows a superior/inferior component to the crossing fibers' route to the contralateral optic tract, similar to the schematic shown in Fig. 7. From these histological sections, one would predict that DTI measurements in the middle central chiasm would contain not only a linear anisotropy component (prolate diffusion displacement profile) in the R/L direction, but also a planar anisotropy component (oblate diffusion displacement profile) with the third eigenvector oriented mostly along the A/P direction corresponding to green pixels on the C_p-ε_3 DEC maps. This predicted diffusion pattern is indeed observed in the central chiasm of the slice most aligned to the referenced histology, Fig. 6E.

From the linear and planar measures, we speculate that the trajectories of crossing fibers have an S/I component that may depend on their dorsal/ventral location in the chiasm. This hypothesis is plausible for several reasons. First, the retinotopic organization is evolving from the optic nerve to the lateral geniculate body. For example, axonal fibers corresponding to rods in the entire nasal hemiretine are destined for layer 1 of the magnocellular system of the lateral geniculate body. Because different fiber populations project to specific layers of the lateral geniculate body, these fibers must group themselves together at some point along their route. It has been shown in Japanese monkeys that retinotopic reorganization not only occurs in the optic nerve, but continues throughout the optic chiasm (Naito, 1994). Secondly, at the boundary of the chiasm, crossing fibers must lose any S/I component, and thus ε_3 aligns with the S/I axis, such that fibers are not projecting outside the boundaries of the structure.

It could be argued that the difference in ε_3 seen at different levels of the optic chiasm arises because the data sets were collected in different scan sessions and simply cut through the crossings at different angles. Indeed, image orientation with the optic chiasm may play a role in our results; however, the difference in the angle of the oblique images compared to the anatomy is on the order of a few degrees, whereas the difference in ε_3 orientation is on the order of tens of degrees. Spurious anisotropy and eigenvector findings may originate from cardiac pulsation. We cannot completely rule out that our optic chiasm findings could be affected in part by cardiac pulsation. However, we found consistent results in the diffusion parameters in the central chiasm regardless of the use of gating.

Acquiring different levels of the optic chiasm in three different scan sessions also highlights the difficulty in achieving intra-subject repeatability with this technique. Because contiguous slices cannot be collected in one acquisition and a single DTI data set at sub-millimeter resolution in this protocol requires lengthy scan times, effectively only a single slice through the optic chiasm can be acquired in one scanning session. Addressing the limitation of not being able to acquire a full volume of the optic chiasm in one session is a current focus of our research. The thin slices and lengthy scan time also pose a problem vis-à-vis subject motion within a scan session. Virtually any through-plane motion causes severe problems at sub-millimeter resolution as the slice of interest may be completely removed from the imaging plane. Subject motion resulting in a loss of the slice of interest occurred in more than half of the unrestrained subjects. Clearly, such a failure rate is too high for clinical studies. Thus, another focus of current research is the reduction in total scan time. In addition, there is the potential to use prospective motion correction systems that can detect and correct for sub-millimeter movement of the head (Zaitsev et al., 2006). With such a system subjects can be unrestrained and comfortably undergo scan sessions of even greater length then presented here, and still acquire the proper slices of interest.

In this study, data was acquired with peripheral gating, when time permitted, for prudence. It is not known if cardiac pulsation affects the region of the optic chiasm and how this non-linear motion, if present, would be manifested in diffusion-weighted radial-FSE. Staempfli et al. performed fiber tracking of the *in vivo* human visual system with and without gating (Staempfli et al., 2007). In their work it is reported that the same tracking results are achieved regardless of trigger delay time or if gating is not used at all. Further investigations of these topics are still needed. One drawback of acquiring data with a cardiac gating method is that the average TR is variable between subjects. In a multi-shot acquisition that is T1-weighted, a change in TR can affect the SNR in the resulting image. It is known that if DTI data has low SNR then the calculated anisotropy measures will be affected (Pierpaoli and Basser, 1996). In the DTI data reported in this study, the SNR of the images is above this low SNR regime. In addition, we found no correlation between the TR used for collecting the DTI data set and the calculated anisotropy or mean diffusivity, therefore we conclude that for relatively long TR values, such as those used in this study, the TR variability introduced by cardiac gating should not be a concern.

There have been reports on DTI's inability to accurately describe complex fiber architecture due to partial volume tissue averaging (Alexander et al., 2001; Tuch et al., 2002). High angular resolution diffusion imaging (HARDI) acquisition methods (Frank 2001; Tuch et al., 2002; Jansons and Alexander, 2003; Ozarslan and Mareci, 2003; Tournier et al., 2004), model-based methods (Assaf et al., 2004), and diffusion spectrum imaging (DSI) (Wedeen et al., 2005) have all been proposed to further elucidate complex architecture. Indeed, these techniques have been shown to uncover multiple fiber crossings within a single voxel. Although HARDI techniques provide information about various fiber populations within a voxel, it is still unknown where within that voxel the fiber populations are located. Furthermore, because tens to hundreds of diffusion directions and/or *b*-values are required to implement these methods, scan times are lengthy and spatial resolution is necessarily low. In this work we have taken the approach of using a more constrained DTI representation of diffusion while improving spatial resolution. We have shown that even a simple DTI measurement can reveal important information about the underlying architecture of a complex structure such as the chiasm. The advantage of high image resolution is an improvement in localization. Typical *in vivo* diffusion data are acquired with SSEPI at 2.5 mm isotropic resolution. Acquiring DTI data at 0.9 mm isotropic resolution effectively provides 21 voxels for each single voxel obtained at 2.5 mm isotropic resolution. The architectural features of fibers in each one of these 21 voxels can be independently assessed by DTI, enabling the characterization of very complex and highly heterogeneous

organizational patterns. A high angular resolution DWI study in theory should improve one's ability to resolve multiple fiber populations in a voxel, but in practice it may not be suitable to investigate complex architectural patterns that vary significantly within a small structure. Although further experimentation and analysis are required, we would argue that for the study of fine anatomical structures with complex architecture, like the optic chiasm, high-resolution DTI is more promising than low resolution HARDI.

Conclusions

In this work, fine details of tissue architecture were elucidated from sub-millimeter *in vivo* DTI data by utilizing our diffusion-weighted radial-FSE sequence for 3 T imaging. Data obtained in the optic chiasm clearly shows the known fiber trajectories through the chiasm, particularly the temporal hemiretinae fibers that remain on the ipsilateral side, and nasal hemiretinae fibers that cross to the contralateral side. In addition, a perimeter of low anisotropy around the medial decussation is consistently observed. We speculate this is a region of complex fiber crossing/divergence/convergence and/or high curvature, where the crossing and uncrossed fiber populations intersect. A considerable planar aspect was also observed in the diffusion ellipsoids of the central optic chiasm, indicating fiber crossings with a component in the S/I direction, rather than strictly R/L. This novel architectural feature suggests that in humans the optic chiasm is a location of dorso-ventral fiber reorganization within the optic pathways, like that known to occur in some animals. The acquisition methods used currently have limited utility due to lengthy scan times. With progress in more efficient data acquisition, these methods may be useful in diagnosing patients with possible visual pathway lesions through sub-millimeter *in vivo* DTI.

Acknowledgments

The authors would like to thank Dr. Cheng Guan Koay for his assistance in implementing the calculation of dispersion measures for the averaged eigenvectors in an ROI. We would like to thank Dr. Peter Basser for his comments and suggestions and Dr. Stefano Marenco for his essential contributions. We would also like to thank Christie Rebsch for her time and efforts put toward this work. The authors thank Liz Salak for editing the manuscript. This study was partly funded by NIMH through protocol 00M0085, V.S. Mattay principal investigator.

References

Alexander, A.L., Hasan, K.M., et al., 2001. Analysis of partial volume effects in diffusion-tensor MRI. Magn. Reson. Med. 45 (5), 770–780.
Assaf, Y., Freidlin, R.Z., et al., 2004. New modeling and experimental framework to characterize hindered and restricted water diffusion in brain white matter. Magn. Reson. Med. 52 (5), 965–978.
Basser, P.J., Pajevic, S., 2000. Statistical artifacts in diffusion tensor MRI (DT-MRI) caused by background noise. Magn. Reson. Med. 44 (1), 41–50.
Basser, P.J., Pierpaoli, C., 1996. Microstructural and physiological features of tissues elucidated by quantitative-diffusion-tensor MRI. J. Magn. Reson., Ser. B 111 (3), 209–219.
Basser, P.J., Mattiello, J., et al., 1994. Estimation of the effective self-diffusion tensor from the NMR spin-echo. J. Magn. Reson., Ser. B 103 (3), 247–254.
Chabert, S., Molko, N., et al., 2005. Diffusion tensor imaging of the human optic nerve using a non-CPMG fast spin echo sequence. J. Magn. Reson. Imaging 22 (2), 307–310.
Frank, L.R., 2001. Anisotropy in high angular resolution diffusion-weighted MRI. Magn. Reson. Med. 45 (6), 935–939.
Jansons, K.M., Alexander, D.C., 2003. Persistent angular structure: new insights from diffusion magnetic resonance imaging data. Inverse Problems 19 (5), 1031–1046.
Jeffery, G., 2001. Architecture of the optic chiasm and the mechanisms that sculpt its development. Physiol. Rev. 81 (4), 1393–1414.
Koay, C.G., Basser, P.J., 2006. Analytically exact correction scheme for signal extraction from noisy magnitude MR signals. J. Magn. Reson. 179 (2), 317–322.
Koay, C.G., Chang, L.C., et al., 2007. Error propagation framework for diffusion tensor imaging via diffusion tensor representations. IEEE Trans. Med. Imag. 26 (8), 1017–1034.
Koay, C.G., Nevo, U., et al., 2008. The elliptical cone of uncertainty and its normalized measures in diffusion tensor imaging. IEEE Trans. Med. Imag. 27 (6), 834–846.
Mattiello, J., Basser, P.J., et al., 1997. The b matrix in diffusion tensor echo-planar imaging. Magn. Reson. Med. 37 (2), 292–300.
Muller-Forell, W., 2004. Intracranial pathology of the visual pathway. Eur. J. Radiol. 49 (2), 143–178.
Naito, J., 1994. Retinogeniculate projection fibers in the monkey optic chiasm: a demonstration of the fiber arrangement by means of wheat germ agglutinin conjugated to horseradish peroxidase. J. Comp. Neurol. 346 (4), 559–571.
Neveu, M.M., Holder, G.E., et al., 2006. Early midline interactions are important in mouse optic chiasm formation but are not critical in man: a significant distinction between man and mouse. Eur. J. Neurosci. 23 (11), 3034–3042.
Ozarslan, E., Mareci, T.H., 2003. Generalized diffusion tensor imaging and analytical relationships between diffusion tensor imaging and high angular resolution diffusion imaging. Magn. Reson. Med. 50 (5), 955–965.
Pajevic, S., Pierpaoli, C., 1999. Color schemes to represent the orientation of anisotropic tissues from diffusion tensor data: Application to white matter fiber tract mapping in the human brain. Magn. Reson. Med. 42 (3), 526–540.
Pell, G.S., Briellmann, R.S., et al., 2006. Optimized clinical T2 relaxometry with a standard CPMG sequence. J. Magn. Reson. Imaging 23 (2), 248–252.
Pierpaoli, C., Basser, P.J., 1996. Toward a quantitative assessment of diffusion anisotropy. Magn. Reson. Med. 36 (6), 893–906.
Pierpaoli, C., Jezzard, P., et al., 1996. Diffusion tensor MR imaging of the human brain. Radiology 201 (3), 637–648.
Pipe, J.G., Farthing, V.G., et al., 2002. Multishot diffusion-weighted FSE using PROPELLER MRI. Magn. Reson. Med. 47 (1), 42–52.
Roebroeck, A., Galuske, R., et al., 2008. High-resolution diffusion tensor imaging and tractography of the human optic chiasm at 9.4†T. NeuroImage 39 (1), 157–168.
Sarlls, J.E., Pierpaoli, C., 2008. Diffusion-weighted radial fast spin-echo for high-resolution diffusion tensor imaging at 3T. Magn. Reson. Med. 60 (2), 270–276.
Staempfli, P., Rienmueller, A., et al., 2007. Reconstruction of the human visual system based on DTI fiber tracking. J. Magn. Reson. Imaging 26 (4), 886–893.
Theilmann, R.J., Gmitro, A.F., et al., 2004. View-ordering in radial fast spin-echo imaging. Magn. Reson. Med. 51 (4), 768–774.
Tournier, J.D., Calamante, F., et al., 2004. Direct estimation of the fiber orientation density function from diffusion-weighted MRI data using spherical deconvolution. NeuroImage 23 (3), 1176–1185.
Trip, S.A., Wheeler-Kingshott, C., et al., 2006. Optic nerve diffusion tensor imaging in optic neuritis. NeuroImage 30 (2), 498–505.
Trouard, T.P., Theilmann, R.J., et al., 1999. High-resolution diffusion imaging with DIFRAD-FSE (diffusion-weighted radial acquisition of data with fast spin-echo) MRI. Magn. Reson. Med. 42 (1), 11–18.
Tuch, D.S., Reese, T.G., et al., 2002. High angular resolution diffusion imaging reveals intravoxel white matter fiber heterogeneity. Magn. Reson. Med. 48 (4), 577–582.
Vinogradov, E., Degenhardt, A., et al., 2005. High-resolution anatomic, diffusion tensor, and magnetization transfer magnetic resonance imaging of the optic chiasm at 3T. J. Magn. Reson. Imaging 22 (2), 302–306.
Wedeen, V.J., Hagmann, P., et al., 2005. Mapping complex tissue architecture with diffusion spectrum magnetic resonance imaging. Magn. Reson. Med. 54 (6), 1377–1386.
Westin, C.F., Maier, S.E., et al., 2002. Processing and visualization for diffusion tensor MRI. Med. Image Anal. 6 (2), 93–108.
Wheeler-Kingshott, C.A.M., Trip, S.A., et al., 2006. In vivo diffusion tensor imaging of the human optic nerve: Pilot study in normal controls. Magn. Reson. Med. 56 (2), 446–451.
Zaitsev, M., Dold, C., et al., 2006. Magnetic resonance imaging of freely moving objects: prospective real-time motion correction using an external optical motion tracking system. NeuroImage 31 (3), 1038–1050.
Zhang, J., Van Zijl, P.C.M., et al., 2006. Image contrast using the secondary and tertiary eigenvectors in diffusion tensor imaging. Magn. Reson. Med. 55 (2), 439–449.